Available online at www.sciencedirect.com
ScienceDirect
Trans. Nonferrous Met. Soc. China 34(2024) 1441−1455
Transactions of Nonferrous Metals Society of China
www.tnmsc.cn

# Linear contraction of sand casting Mg−9Gd−3Y−0.5Zr alloy

Rui JIANG[1], Guo-hua WU[1], He XIE[1], Xin TONG[1], Liang ZHANG[1], Fang-zhou QI[1], Wen-cai LIU[1], Ying-jing GENG[2], Guang-xiao REN[2]

1. National Engineering Research Center of Light Alloy Net Forming and State Key Laboratory of Metal Matrix Composite, School of Materials Science and Engineering, Shanghai Jiao Tong University, Shanghai 200240, China;
2. Shanxi Jianghuai Heavy Industry Co., Ltd., Jincheng 048000, China

Received 9 October 2022; accepted 23 March 2023

**Abstract:** The effect of geometric characteristics of castings on the linear contraction of sand casting Mg−9Gd−3Y−0.5Zr alloy (VW93) was studied. The dimensions of free and restrained structure castings were precisely extracted by a 3D scanner and then used for the calculation of the contraction coefficient. The ratio of sand core volume to enveloping volume of casting ($\gamma$), was introduced to quantify the degree of constraint caused by sand cores. According to the statistical distribution of free contraction coefficients and the evolution of restrained contraction coefficients against $\gamma$, it is indicated that the free contraction coefficient of VW93 alloy equals 1.96%, and the restrained contraction coefficient declines linearly with the increasing $\gamma$, which supplies support on predicting the contraction of VW93 alloy through the geometric characteristic of castings.

**Key words:** free contraction; restrained contraction; sand casting; Mg−9Gd−3Y−0.5Zr alloy

## 1 Introduction

Magnesium alloys with high content of rare earth elements possessing high specific strength and heat resistance have been attracting large amounts of investigations [1,2] on the microstructure evolution [3−5], strengthening mechanism [6−8], and failure behavior [9], driving remarkable applications [10,11] of these alloys in aerospace manufacturing. For an instance, Mg−9Gd−3Y−0.5Zr alloy has been applied as the structure material for key equipment of some aircraft. However, the challenge of ensuring dimensional compliance remains in the process of sand casting that is considered as the primary method of fabricating the alloys into engineering parts [12,13]. For large and complex parts formed by sand casting, the dimensional deviation of the castings brings obstructs into subsequent machining adjustment and even leads to the scrapping of the parts [14]. Contraction of the alloy upon solidification and cooling is the primary reason for dimensional changes [15,16]. The key of dimension control of casting requires finding a way or model to evaluate the amount of its contraction, which is known as the pattern allowance (PA, $A_P$) [14,17]:

$$A_P = \frac{L_M - L_C}{L_M} \times 100\% \quad (1)$$

where $L_M$ and $L_C$ are the dimensions of pattern and casting, respectively. According to this equation, $L_C$ equals $L_M(1-A_P)$. Apparently, $L_C$ depends on $L_M$ upon solidification and contraction of the casting during solidification and cooling. Every procedure from pouring to cooling is a potential factor that affects

**Corresponding author:** Guo-hua WU, Tel: +86-21-54742630, E-mail: ghwu@sjtu.edu.cn;
Liang ZHANG, Tel: +86-21-54742630, E-mail: liangzhang08@sjtu.edu.cn
DOI: 10.1016/S1003-6326(24)66482-4
1003-6326/© 2024 The Nonferrous Metals Society of China. Published by Elsevier Ltd & Science Press
This is an open access article under the CC BY-NC-ND license (http://creativecommons.org/licenses/by-nc-nd/4.0/)

the dimension of the casting [18,19], so error arising from PA can sometimes be corrected over a long development period. In the production process, the control of $L_C$ relies on a time-consuming trial-and-error method that requires several design iterations. Such modification on dimension contributes much hidden part of the cost of a qualified product. Therefore, the appropriate assignment of PA for Mg−9Gd−3Y−0.5Zr alloy has vital importance to promote its engineering application.

However, little direct research on the contraction behavior of sand casting Mg−9Gd−3Y−0.5Zr alloy was reported. The investigations on the nature and causes of dimension errors in the sand casting of steels [14,17], cast irons [20−22] and aluminum alloys [23,24] have paid focus on the influence of casting geometry and mold restraint and their interaction on the contraction behavior of feature dimensions. KOCHAR [25] quantified the impact of casting geometry and process variables on the PA of steel and pointed out that the variation due to the effect of geometry has a larger effect than the variation due to the process. The envelope density was proposed by CAMPBELL [26] to evaluate the constrained contraction as a function of casting geometry. In addition, CAMBELL et al studied the influence of the degree of mold constraint on the PA of grey iron [20], ductile iron [21], and aluminum alloy [24]. Their experiments were carried out by casting a series of slender bars with flanges on both sides to induce mold constraint, demonstrating that the PA of grey iron, ductile iron, and aluminum alloy decreased with the increase of the degree of mold constraint. The mechanical interaction between casting and mold was also responsible for the dimensional changes of casting and has been the focus of previous studies [27−30]. MOTOYAMA et al [29] measured the dynamical dimensional changes of the casting and the load on the casting from sand mold by using a linear variable differential transformer (LVDT), and found that the increase of dimensional contraction as well as the release of contraction stress occurred abruptly upon the shake-out of sand mold. GALLES and BECKERMANN [14] studied the effect of core expansion on distortions during steel casting by measuring the evolution of the cylinder's internal diameter using LVDT. The sand dilation due to the shear stress instead of thermal expansion was found to be the dominant factor of the increase in the internal diameter.

Although little direct research on the contraction behavior of Mg−9Gd−3Y−0.5Zr alloy during sand casting was carried out, the previous studies on other alloys suggest that the casting geometry and mold constraint account for the majority of the dimensional changes of casting. In this work, the influence of casting geometry and mold constraint on the linear contraction of Mg−9Gd−3Y−0.5Zr alloy was studied, and the evolution of PA against geometric features under free and restrained contraction was determined, which may provide a guidance for dimension control of large and complex Mg−RE alloy parts manufactured by sand casting.

## 2 Experimental

The present study focused on the determination of PA for a series of structures containing cubic blocks, cylinders, hollow cylinders, "I"-shapes, and frames, produced in furan resin sand molds. Experimental procedures consist of pattern design, mold preparation, melt preparation, dimension measurements, and the measurement of the coefficient of thermal expansion (CTE).

### 2.1 Pattern design

Pattern design is illustrated in Fig. 1. Two types of pattern are designed: free contraction shapes and constrained contraction shapes. The first pattern consists of 8 cubic blocks (C1−C8) and 3 mm cylinders (R1−R3), as shown in Fig. 1(a). Blocks (C1−C5) possess the same cross-section (60 mm × 50 mm) and have an incremental length from 200 to 400 mm (with an increment of 50 mm). Blocks (C5−C8) and cylinders (R1−R3) are of equal volume but have varying cross-sections and lengths. The dimensions of blocks and cylinders are shown in Table 1 and Table 2, respectively. As shown in Fig. 1(b), the second pattern contains 5 frames (F1−F5), 2 hollow cylinders (R4 and R5), and 2 "I"-shaped bars (G1 and G2). All patterns have a height of 60 mm, frames (F1, F2, F4 and F5) have the same thickness of 25 mm, and hollow cylinders have the same external diameter of 160 mm. All dimensions marked in Fig. 1(b) are shown in Table 3 (for F1−F5, G1 and G2) and Table 4 (for R4 and R5).

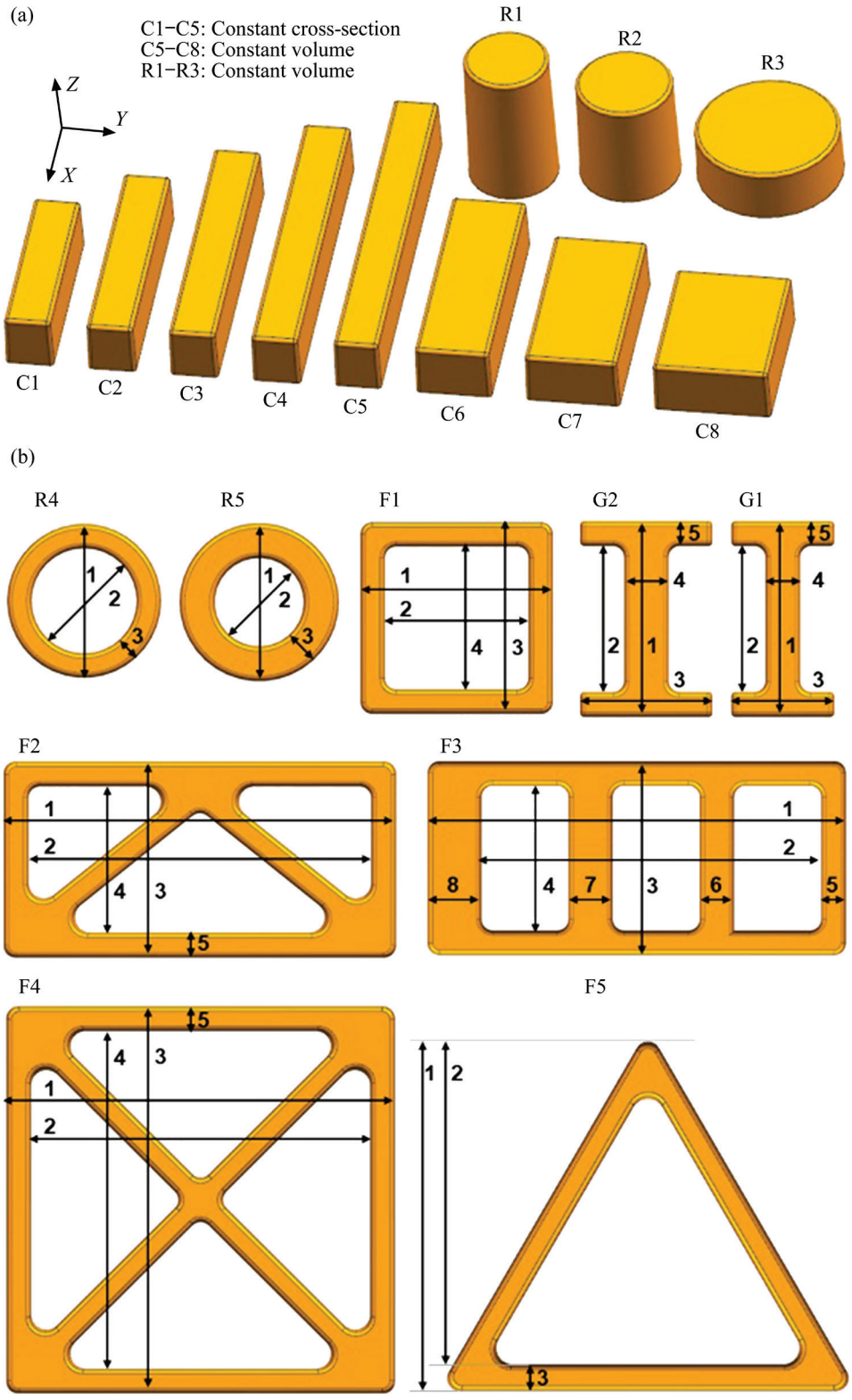


**Fig. 1** Design of free (a) and constrained (b) contraction patterns (The dimensions of C1−C8 along directions *X*, *Y* and *Z* are shown in Table 1, and the diameter and height of R1−R3 are shown in Table 2. The dimensions marked by arrows with a number in (b) are shown in Table 3 (F1−F5, G1 and G2) and Table 4 (R4 and R5))

### 2.2 Mold preparation

The molds were prepared with furan resin sand and the gating system was designed as illustrated in Fig. 2, where the height of the sprue and runner is 60 mm and the width of the ingate is 20 mm.

**Table 1** Mold dimensions and PA values along directions *X*, *Y* and *Z* and volume contraction of C1−C8

| No. | Direction *X* | | Direction *Y* | | Direction *Z* | | Volume | |
|---|---|---|---|---|---|---|---|---|
| | $L_M$/mm | PA (S.D.)/% | $L_M$/mm | PA (S.D.)/% | $L_M$/mm | PA (S.D.)/% | $V_M$/mm$^3$ | PA/% |
| C1 | 201.15 | 1.84 (0.12) | 50.61 | 2.89 (0.97) | 60.00 | 0.57 (0.51) | 613352 | 5.50 |
| C2 | 250.24 | 1.91 (0.20) | 50.35 | 2.74 (0.41) | 60.00 | 1.38 (0.51) | 766177 | 6.26 |
| C3 | 300.29 | 1.80 (0.11) | 50.79 | 2.58 (0.27) | 60.00 | 0.90 (0.62) | 918989 | 5.44 |
| C4 | 351.90 | 2.01 (0.05) | 51.84 | 1.70 (0.60) | 60.00 | 0.95 (0.57) | 1071801 | 4.90 |
| C5 | 398.95 | 1.91 (0.12) | 48.21 | 3.46 (0.49) | 60.00 | 0.08 (0.58) | 1168087 | 5.37 |
| C6 | 251.06 | 2.05 (0.36) | 81.89 | 2.17 (0.32) | 60.00 | 1.15 (0.61) | 1217864 | 4.88 |
| C7 | 200.89 | 1.66 (0.09) | 100.41 | 2.02 (0.42) | 60.00 | 1.57 (1.38) | 1210281 | 5.59 |
| C8 | 161.13 | 2.16 (0.07) | 125.77 | 2.18 (0.22) | 60.00 | 1.37 (1.42) | 1215333 | 5.57 |

**Table 2** Mold dimensions and PA values of radius and height and volume contraction of R1−R3

| No. | Diameter | | Height | | Volume | | *H*/*D* |
|---|---|---|---|---|---|---|---|
| | $L_M$/mm | PA (S.D.)/% | $L_M$/mm | PA (S.D.)/% | $V_M$/mm$^3$ | PA/% | |
| R1 | 97.30 | 3.36 (0.34) | 160 | 1.69 (0.14) | 1138454 | 8.54 | 1.64 |
| R2 | 109.44 | 3.24 (0.39) | 125 | 1.98(0.27) | 1140366 | 8.21 | 1.14 |
| R3 | 159.76 | 2.11 (0.07) | 60 | 1.75 (1.19) | 1189030 | 5.50 | 0.38 |

**Table 3** Volume shrinkage, linear contraction for dimensions (Fig. 1(b)), and CVF of frames and "I"-shaped bars

| Dimension | | F1 | F2 | F3 | F4 | F5 | G1 | G2 |
|---|---|---|---|---|---|---|---|---|
| Volume | $V_M$/mm$^3$ | 1002827 | 2327371 | 2652572 | 3651270 | 1456874 | 609968 | 786494 |
| | PA/% | 5.85 | 5.19 | 6.72 | 6.04 | 5.68 | 5.49 | 5.14 |
| Height | $L_M$/mm | 60 | 60 | 60 | 60 | 60 | 60 | 60 |
| | PA (S.D.)/% | 0.62 (1.05) | 0.22 (0.52) | 1.59 (1.05) | 0.37 (0.85) | 0.91 (0.06) | 0.09 (0.29) | 0.17 (0.39) |
| 1 | $L_M$/mm | 199.83 | 399.82 | 429.76 | 399.82 | 334.13 | 199.83 | 199.83 |
| | PA (S.D.)/% | 1.71 (0.19) | 1.47 (0.05) | 1.64 (0.24) | 1.43 (0.09) | 1.50 (0.11) | 1.67 (0.09) | 1.71 (0.06) |
| 2 | $L_M$/mm | 150.17 | 350.18 | 350.19 | 350.19 | 255.70 | 150.17 | 150.17 |
| | PA (S.D.)/% | 1.16 (0.10) | 1.31 (0.08) | 1.24 (0.10) | 1.16 (0.11) | 1.27 (0.12) | 1.36 (0.09) | 1.32 (0.14) |
| 3 | $L_M$/mm | 199.83 | 199.82 | 199.80 | 399.82 | 24.83 | 104.82 | 134.82 |
| | PA (S.D.)/% | 1.61 (0.14) | 1.50 (0.16) | 1.87 (0.11) | 1.47 (0.06) | 2.26 (0.55) | 2.40 (0.22) | 2.00 (008) |
| 4 | $L_M$/mm | 150.17 | 150.17 | 150.23 | 350.19 | | 34.83 | 44.83 |
| | PA (S.D.)/% | 1.26 (0.17) | 1.25 (0.06) | 1.29 (0.12) | 1.25 (0.07) | | 3.91 (0.76) | 3.23 (0.93) |
| 5 | $L_M$/mm | 24.83 | 24.83 | 24.83 | 24.83 | | 24.82 | 24.82 |
| | PA (S.D.)/% | 3.55 (0.79) | 2.63 (0.54) | 3.64 (0.49) | 3.32 (0.73) | | 2.66 (0.25) | 2.86 (0.61) |
| 6 | $L_M$/mm | | | 34.81 | | | | |
| | PA (S.D.)/% | | | 2.55 (1.51) | | | | |
| 7 | $L_M$/mm | | | 44.81 | | | | |
| | PA (S.D.)/% | | | 3.02 (1.93) | | | | |
| 8 | $L_M$/mm | | | 54.82 | | | | |
| | PA (S.D.)/% | | | 3.47 (2.19) | | | | |
| | CVF | 0.5815 | 0.5129 | 0.4851 | 0.6193 | 0.5943 | 0.5159 | 0.5145 |

The numbers 1−8 correspond to the dimensions shown in Fig. 1(b); CVF means core volume factor

**Table 4** Linear and volume shrinkage of hollow cylinders (R4 and R5)

| No. | External radius | | Internal radius | | Wall thickness | | Height | | Volume | | CVF |
|---|---|---|---|---|---|---|---|---|---|---|---|
| | $L_M$/mm | PA (S.D.)/% | $L_M$/mm | PA (S.D.)/% | $L_M$/mm | PA (S.D.)/% | $L_M$/mm | PA (S.D.)/% | $V_M$/mm$^3$ | PA/% | |
| R4 | 159.76 | 1.99 (0.06) | 110.24 | 1.34 (0.12) | 49.52 | 3.46 (0.27) | 60 | 1.02 (0.66) | 606725 | 6.95 | 0.4624 |
| R5 | 159.76 | 2.05 (0.08) | 89.15 | 1.23 (0.02) | 69.52 | 3.14 (0.19) | 60 | 1.13 (0.33) | 797402 | 6.36 | 0.3136 |

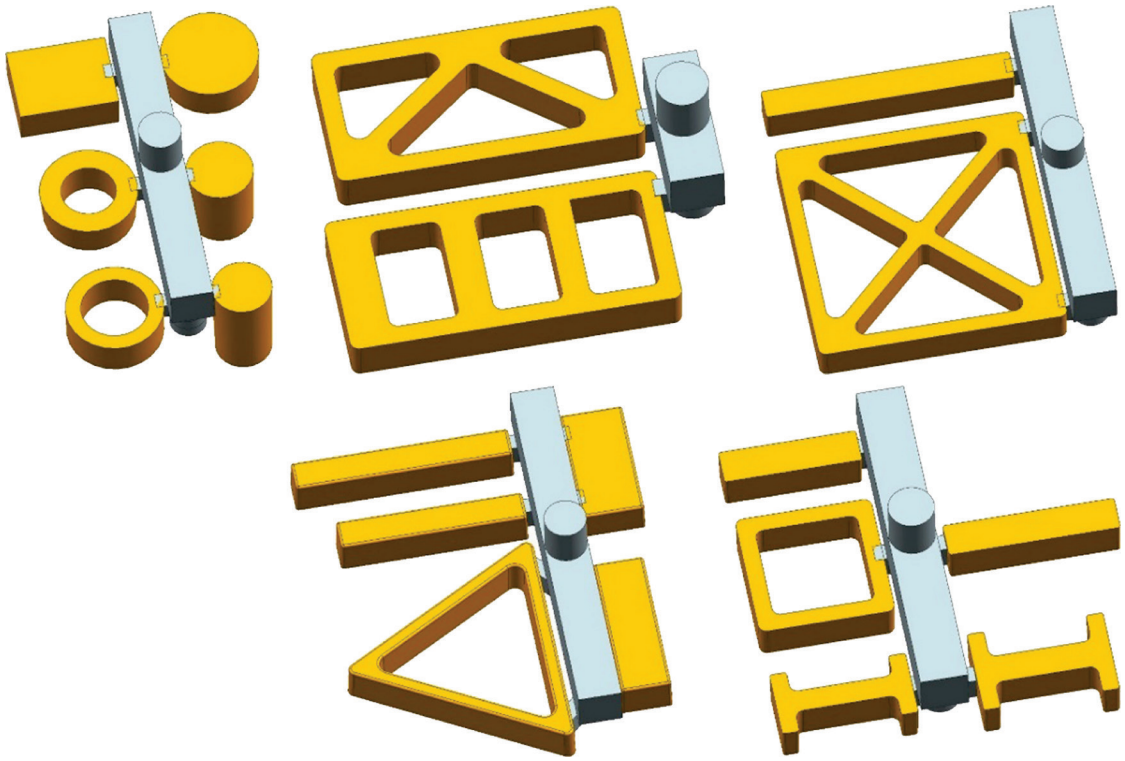

**Fig. 2** Design of gating system (Sprues and runners have same height (60 mm), and ingates have same width (20 mm) and height (30 mm))

### 2.3 Melt preparation

60 kg of pure Mg (99.9%) and master alloys containing Mg−87Gd (wt.%), Mg−90Y, and Mg−30Zr were melted in a steel crucible heated by a well-resistance furnace. The mixing atmosphere of $CO_2$ and $SF_6$ was employed to protect the melt from burning. After holding at 750 °C for 10 min, the melt was poured into sand molds. A separate chill cast sample was taken from the ladle and used to analyze the chemical composition determined by inductively couple plasma-atomic emission spectroscopy (ICP-AES).

### 2.4 Dimension measurement

Conventional dimensional detection methods (measurement tapes and calipers) inevitably introduce the measurement errors that bring confounding to the determination of dimensional changes. To minimize the measurement error, the present work employed a 3D scanner (HScan771 with an accuracy of 0.02 mm) to collect and merge space points from the measured shapes, constructing their digital 3D models from which the geometric information including dimension and volume was extracted. Based on the constructed 3D models, 7 sets of data were measured for each dimension of the studied shapes (see Fig. 3) to perform further analysis.

### 2.5 Measurement of CTE

The CTE value of the studied alloy was tested by thermal dilatometer (DIL 402 Expedis) from 25 to 500 °C.

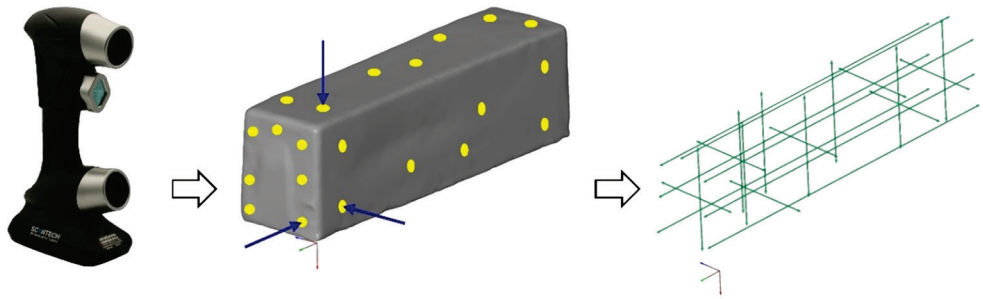


**Fig. 3** Process of dimension extraction from constructed digital 3D model

## 3 Results

The chemical composition of the studied alloy is Mg−9.2Gd−3.1Y−0.5Zr in line with expectations. All castings containing C1−C8, R1−R5, F1−F5, G1, and G2 are complete without lack of flesh, as shown in Fig. S1 (Supplementary materials). The mean value of CTE of the studied alloy is $30.15\times10^{-6}$ $K^{-1}$, as shown in Fig. 4.

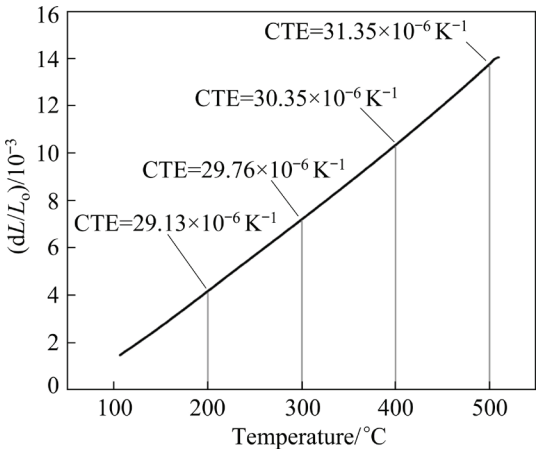


**Fig. 4** Coefficient of thermal expansion (CTE) of Mg−9.2Gd−3.1Y−0.5Zr alloy

### 3.1 Linear and volume contraction of free contraction structures

The dimension comparisons between the castings (C1−C8) and molds along *X*, *Y*, and *Z* directions are shown in Fig. 5, and specific values of PA and volume contraction are filled in Table 1. As displayed in Fig. 5, the amount of contraction for C1−C8 gradually increases with the increase of the dimension along *X* direction, and fluctuates within a certain range along *Y* and *Z* directions, especially along *Z* direction, the dimension of casting within some parts (yellow in Fig. 5) is even larger than the mold. As shown in Table 1, the different ranges of specific values of PA for dimensions along *X*, *Y* and *Z* directions as well as volume contraction are observed. For C1−C5 blocks with the same cross-section, the values of PA along *X* direction fall within the range of 1.80%−2.01%, but those along *Y* and *Z* directions fall within the range of 1.70%−3.46% and 0.08%−1.38%, respectively, both of which are wider than that along *X* direction. For C5−C8 blocks with the same volume and varying cross-sections, the range of PA along *X* direction is 1.66%−2.16% and those along *Y* and *Z* directions are 2.02%−3.46% and 0.08%−1.57%, respectively. The volume shrinkage rate fluctuates in the range of 4.88%−5.59%. Apparently, the ranges of PA for the longer dimensions show a weaker fluctuation.

The dimension comparisons between the castings (R1−R3) and molds along radial direction and height are shown in Fig. 6, in which the color depth indicates the degree of dimensional contraction of the castings relative to corresponding molds based on the reference plane (alignment plane) and reference axis (alignment axis). Specific values of PA and volume contraction are listed in Table 2. As the radius grows from R1 to R3, the amount of contraction does not increase gradually, which is distinct from that of C1−C8. According to the results from Table 2, both values of PA along the radial direction and volume contraction decrease from R1 to R3, but the values of contraction along height fluctuate are in the range of 1.69%−1.98%. Noticeably, the ratio of height to diameter (*H*/*D*) has non-negligible influence on the decrease of radial PA and volume contraction. As the value of *H*/*D* decreases, the decrease of radial PA and volume contraction from R2 to R3 is more significant than that from R1 to R2. Compared with

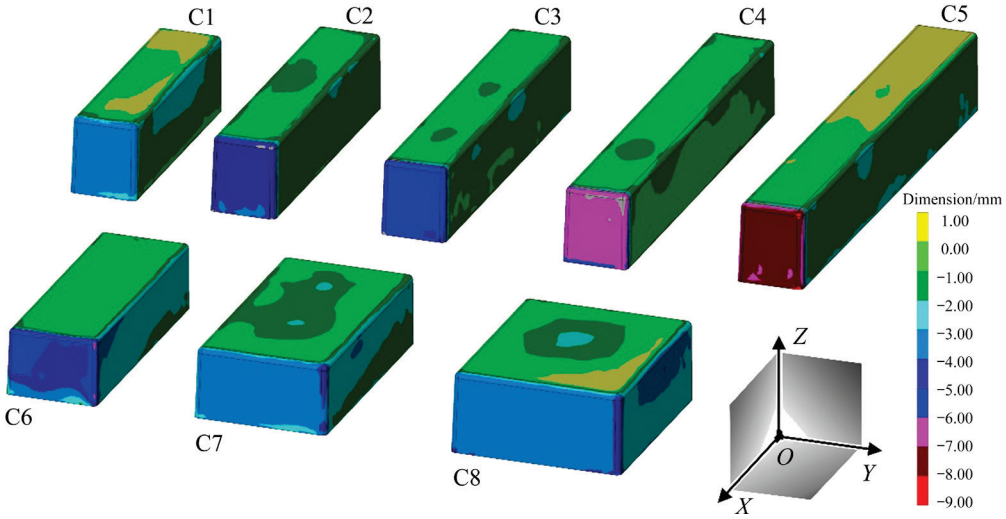


**Fig. 5** Dimensional comparison between castings (C1−C8) and molds (The color depth indicates the degree of dimensional contraction of the castings relative to corresponding molds based on the reference plane (alignment plane) *XOY*, *XOZ* and *YOZ*)

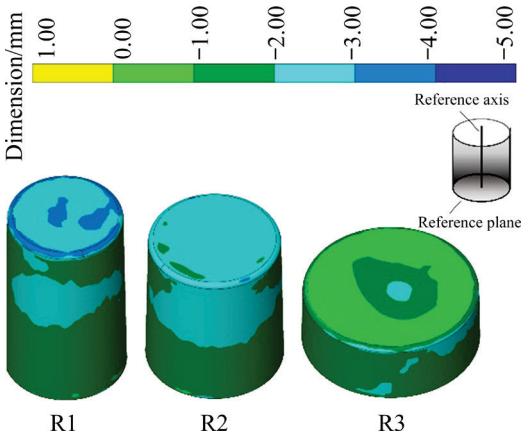


**Fig. 6** Dimensional comparison between castings and responding molds

blocks (C5−C8) with similar volume, R1 and R2 cylinders have larger volume contraction, but R3 cylinder has volume contraction with the same level.

### 3.2 Linear and volume contraction of constrained contraction structures

The degree of contraction for frames with different structures is displayed in Fig. 7, in which the color depth indicates the degree of dimensional contraction of the castings relative to corresponding patterns based on the reference plane of (alignment plane) *XOY*, *XOZ* and *YOZ*. Specific values of PA for dimensions marked in Fig. 1(b) and volume contraction are shown in Table 3. It should be noted that constrained contraction occurs on dimensions that pass through the sand core, such as the dimensions marked with 1 in Fig. 1, and free contraction occurs on dimensions that do not pass through the sand core, such as height and wall thickness. Compared with free contraction blocks with the same dimension, the amount of contraction of frames (F2, F3, F4 and F5) along *Y* direction is less than that of C5 due to restraint by the sand core. Although both height and wall thickness contract without restraint, the contraction values of them are different. The contraction values of height for all frames fluctuate in the range of 0.09%−1.59%, but those of wall thickness are in the range of 2.26%−3.64%. While considering restrained contraction, external and internal dimensions are worth attention. For example, the dimension marked with 1 for F1 is the external dimension and the one marked with 2 is the internal dimension. The contraction of the external dimension contains that of internal dimensions and wall thickness. From the data in Table 3, the contraction of the internal dimension for each frame is lower than that of the external dimension. Except the common phenomena above, some vital but latent rules deserve attention. The structures of F1, F2, F3, G1, and G2 have the same external and internal dimensions along *Y* direction (dimensions 1 and 2 of F1, G1 and G2, and dimensions 3 and 4 of F2 and F3), but show different values of contraction.

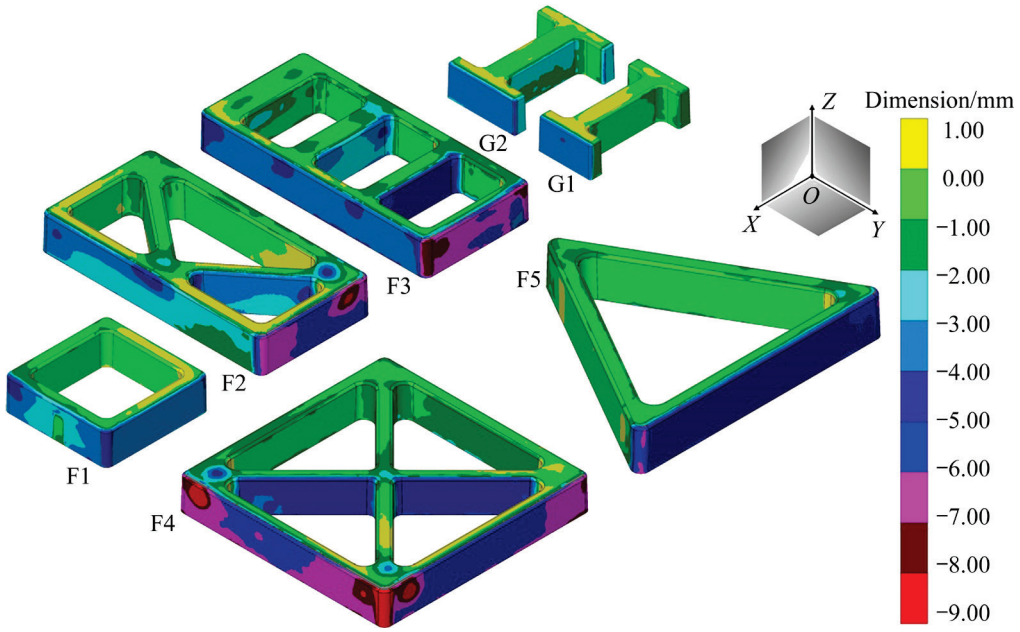


**Fig. 7** Dimensional comparison between restrained castings and corresponding molds

The same is true for dimensions of F2, F3 and F4 structures along $X$ direction. The correlation between restrained contraction and geometric characteristics is revealed in the discussion section.

The dimension comparisons between the castings (R4, R5) and molds along radial direction and height are shown in Fig. 8. Table 4 shows the contraction values for external radius, internal radius, wall thickness, and volume of hollow cylinders R4 and R5. Due to the restraint of the sand core, the PA of the external diameter for both R4 and R5 is lower than that of R3 having the same diameter. Although R4 has a larger internal radius than R5, which means that the radius contraction of R4 is restrained by a larger sand core than R5, the value of the internal radius contraction of R4 is unexpectedly higher than that of R5. The contraction of wall thickness is not restrained, and so shows a larger value than external and internal diameters. The volume contraction of R4 and R5 is larger than that of R3 and decreases with the decrease of internal diameter, exhibiting a similar trend to the contraction change of wall thickness.

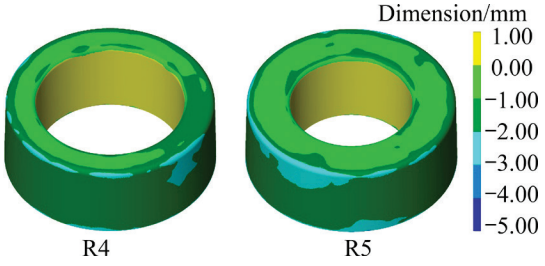


**Fig. 8** Dimensional comparison between castings (R4, R5) and responding molds

## 4 Discussion

From the above experimental results, fluctuations of the contraction of dimensions for all the studied structures containing unrestrained features (C1−C8 and R1−R3) and restrained features (F1−F5, R4, R5, and G1, G2) found the common phenomena. And the contractions along different directions fall within different ranges that are dependent on the geometric characteristics, and errors during the casting and measuring process. In this section, the influences of errors and geometric characteristics on the contraction of unrestrained and restrained features are discussed, the distribution of unrestrained contraction is revealed, and the determination method for restrained contraction is established.

### 4.1 Distribution and ideal value of free contraction

There are many highly interdependent physical processes responsible for the studied alloy castings not having the same dimensions as the pattern from which the molds are made. Contraction of the alloy upon solidification and cooling to room temperature

(solid contraction) is the primary reason for dimensional changes. The degree of the solidification contraction is dependent on the feeding pressure. Considering the unrestrained features were poured through the same gating system providing the similar/same pouring pressure, it can be assumed that the solidification contraction of Blocks C1−C8 is a fixed value. And the rest solid contraction ($S_C$) is calculated by

$$S_C=\alpha(T_S-T_{room}) \quad (2)$$

where $\alpha$ is the thermal expansion coefficient of the alloy, $T_S$ and $T_{room}$ are the solidus temperature of the alloy and room temperature, respectively. Given that the value of $\alpha$ is $3.09\times10^{-5}\,K^{-1}$ obtained from Fig. 4 and the solidus temperature of the alloy was 570 °C [3], the value of $S_C$ equals 1.68% which is also a fixed value. By adding up those two parts of contraction (solidification and solid contraction), the obtained free contraction for Blocks C1−C8 should ideally be a fixed value higher than $S_C$. In fact, the values of free contraction measured in this experiment are all higher than $S_C$, but fluctuate within a certain range. Necessarily, the reasons that the free contraction fluctuates should be dug out, are worth attention.

From the previous reports of MKUMBO et al [20] and NYICHOMBA et al [21], the free contraction of ductile iron and gray cast iron was in negative correlation with the casting modulus. However, no similar correlation between the casting modulus of Blocks C1−C8 and the values of free contraction was found (Fig. S2) in this work. Essentially, the casting modulus reflects the cooling rate and a larger modulus indicates a lower cooling rate. A possible explanation for this is that the solidus temperature of ductile iron and gray cast iron is much higher than that of the studied alloy. GALLES [31] and MANDAR [32] suggested that the free contraction of steel casting with varying dimensions exhibited different distribution ranges, which is similar to our findings. In this work, the measured contraction from castings C1−C8 was plotted over a range of feature lengths, as shown in Fig. 9(a). The considerable scatter of PA demonstrates that, as feature length increases, the values of PA converge towards 2.0% that is much close to 1.95%, the mean value is obtained from the statistical results (Fig. 9(b)). Such a distribution trend centered at 2.0% indicates that there are a few

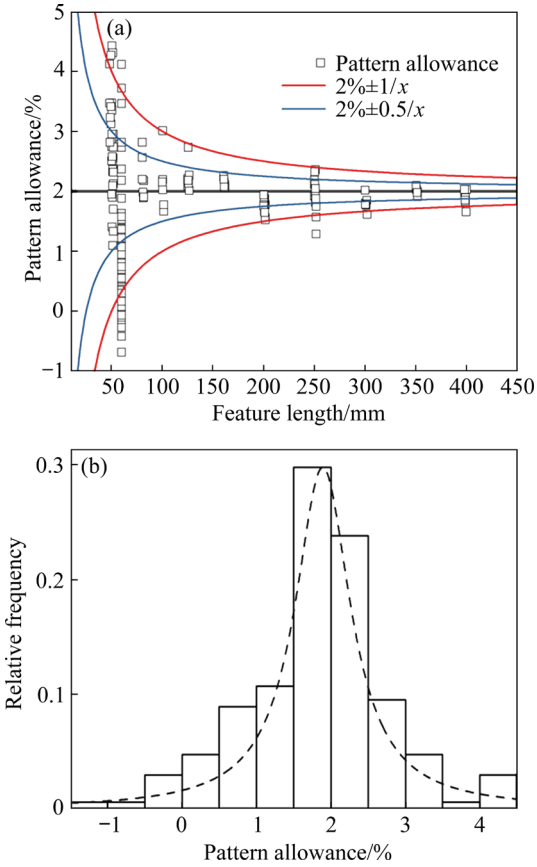


**Fig. 9** Distribution trend of measured PA along different directions (a) and statistical results for C1−C8 (b) ($1/x$ indicates the effect of random error determined by casting environment)

errors affecting the determination of PA.

The degree of influence of errors on the distribution of PA is determined by Eq. (1), where the change of 0.5 and 1 mm in the molecule is capable to cause PA fluctuating within the range shown by the blue and red lines in Fig. 9(a), respectively. More than 90% of scatters of PA are concentrated below the boundary of $2\%\pm1/x$ and a change of 0.5−1 mm is sufficient to deviate the PA for dimensions lower than 100 mm from 2% to the range of 3%−4%. Therefore, variations in mold dimensions and measurement errors for casting dimensions deliver non-negligible effects on the value of PA. However, while calculating the values of PA by Eq. (1), the direct use of $L_M$ and $L_C$ inevitably introduces two types of errors, of which one results from the uneven thickness of the coating on the surface of the sand mold, and the other emerges during the process of measuring $L_C$. To obtain the ideal PA*, the following Eq. (3) should be used:

$$A_{\mathrm{P}}^{*}=\frac{L_{\mathrm{M}}^{*}-L_{\mathrm{C}}^{*}}{L_{\mathrm{M}}^{*}}=\frac{\left(L_{\mathrm{M}}+\Delta L_{\mathrm{M}}\right)-\left(L_{\mathrm{C}}+\Delta L_{\mathrm{C}}\right)}{L_{\mathrm{M}}+\Delta L_{\mathrm{M}}} \tag{3}$$

where $L_{\mathrm{M}}^{*}$ is the initial dimension of mold upon solidification of alloy, $L_{\mathrm{C}}^{*}$ is the non-error dimension of casting, $\Delta L_{\mathrm{M}}$ is the error between $L_{\mathrm{M}}$ and $L_{\mathrm{M}}$*, and $\Delta L_{\mathrm{C}}$ is the measurement error between $L_{\mathrm{C}}$ and $L_{\mathrm{C}}^{*}$. After rearranging Eq. (3), the relation between $L_{\mathrm{C}}$ and $L_{\mathrm{M}}$ and the corresponding error is established as

$$L_{\mathrm{C}}=L_{\mathrm{M}}(1-A_{\mathrm{P}}^{*})+\Delta L_{\mathrm{M}}(1-A_{\mathrm{P}}^{*})-\Delta L_{\mathrm{C}} \tag{4}$$

Equation (4) shows the correlation between $L_{\mathrm{C}}$ and $L_{\mathrm{M}}$, and $1-A_{\mathrm{P}}^{*}$ and $\Delta L_{\mathrm{M}}(1-A_{\mathrm{P}}^{*})-\Delta L_{\mathrm{C}}$ serve as slope and intercept, respectively. By fitting the linear relationship between measured scatters of $L_{\mathrm{C}}$ and $L_{\mathrm{M}}$, $A_{\mathrm{P}}^{*}$ and the statistical value of the errors contained in measured scatters are obtained with the aid of slope and intercept. As shown in Fig. 10, the fitting result for Blocks C1−C8 shows a function of $L_{\mathrm{C}}$=0.9805$L_{\mathrm{M}}$+0.1209, from which $A_{\mathrm{P}}^{*}$ equals 1−0.9805=0.0195 and the statistical value of error is 0.1209.

In order to further analyze the effect of the error on PA, the comparison between measured contraction and ideal contraction is operated and shown in Fig. 11. In Fig. 11, the ideal relation between $L_{\mathrm{C}}^{*}$ and $L_{\mathrm{M}}^{*}$ is plotted as a line (ideal line) that follows the formula $L_{\mathrm{C}}^{*}$=0.9805$L_{\mathrm{M}}^{*}$, and measured data are plotted as scatters. $\Delta L_{\mathrm{C}}$ and $\Delta L_{\mathrm{M}}$ cause the deviation of the scatters from the ideal line in the $Y$-axis direction (vertical error) and $X$-axis direction (horizontal error), respectively. Known

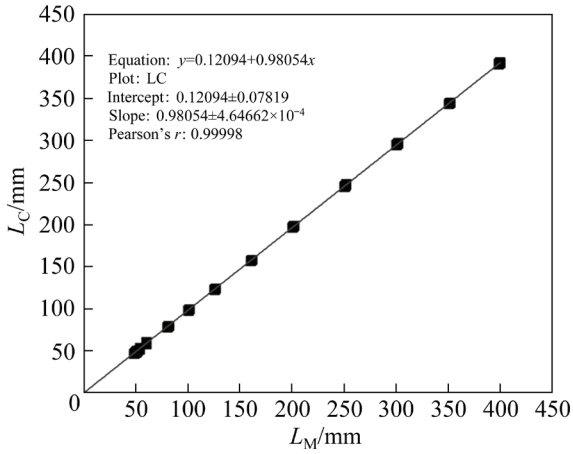


**Fig. 10** Linear fitting result between $L_{\mathrm{C}}$ and $L_{\mathrm{M}}$ for blocks C1−C8

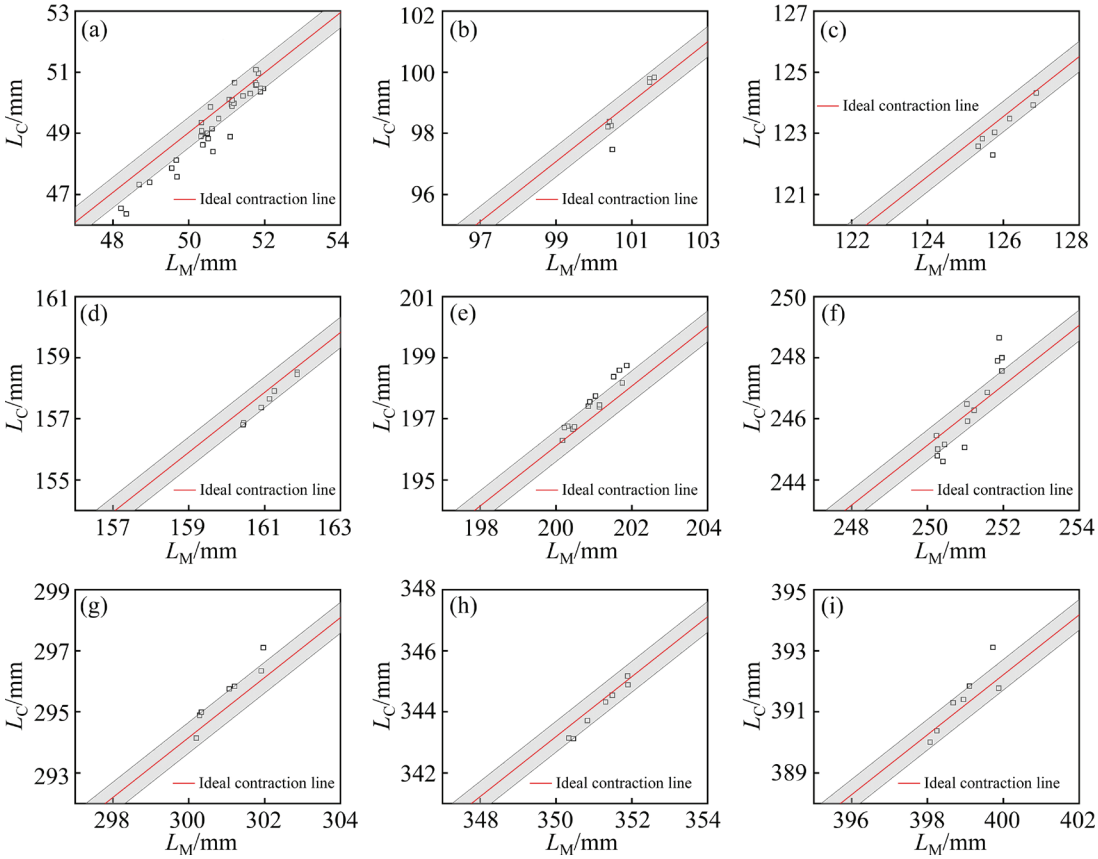


**Fig. 11** Comparison between measured contraction and ideal contraction for C1−C8 blocks (The red line represents the ideal contraction formula $L_{\mathrm{C}}^{*}$= 0.9805$L_{\mathrm{M}}^{*}$, and scatters represent the measured data)

that the accuracy of 3D scanner is 0.02 mm/m, that is to say, $\Delta L_C$ equals 0.02 mm that can be neglected. Therefore, the primary reason that scatters deviate from the ideal line is the horizontal error. In the range of 50−400 mm, most of the scatters are distributed within a 1 mm-wide error band centered on the ideal line. Interestingly, the coating on the surface of the sand mold has a thickness in the range of 0−0.6 mm (Fig. S2), which is comparable to half of the width of the error band surrounding the ideal line. Combined with the results in Fig. 8, it can be considered that the dimension change of sand mold caused by the thickness of the coating has a non-negligible effect on the determination of the PA, especially for the short dimensions.

### 4.2 Influence of height-to-diameter ratio on contraction of R1−R3 cylinders

There are similarities and differences between the contraction of cylinders (R1−R3) and blocks (C1−C8). As shown in Fig. 12(a), the triangular marks distribute in the band of C1−C8, indicating that the contraction of cylinders R1−R3 along the height direction is under the same law as C1−C8 blocks. The same is true for the radial contraction of R3. While some of the circle marks are significantly beyond the band of C1−C8, demonstrating that the radial contraction of cylinders R1 and R2 is different from the contraction law of C1−C8. Considering that R1−R3 cylinders and C1−C8 blocks in this experiment were formed in the same casting environment, it can be considered that process errors (including mold size changes and measurement errors) have the same effect on the PA values of them, so the radial contraction for cylinders R1 and R2 deviates from the distribution band for other reasons. R1−R3 are similar in volume but different from the *H*/*D* ratio, which has a significant effect on the radical contraction decrease (see Fig. 12(b)). The cylinder with a higher ratio of *H*/*D* has higher casting modulus and the increase in contraction values with increasing *H*/*D* value is likely due to the fact that increased time for plastic deformation and creep of the casting leads to decreased contraction.

### 4.3 Influence of geometric characteristics on shrinkage of restrained structures

As mentioned in Section 2.2, the contraction for Frames F1−F5 and "I"-beams G1 and G2 is

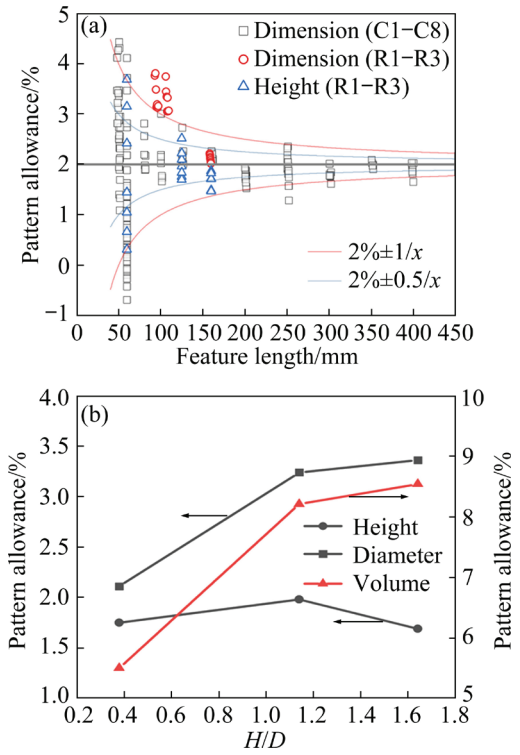


**Fig. 12** Distribution law of shrinkage rate in radial and height directions of cylinder (a) and shrinkage rate of cylinder in height-to-diameter ratio (b)

quantified through internal, external, and thickness dimensions. Here, the values of PA for the above three dimensions are found in three branches of the distribution band of C1−C8, as revealed in Fig. 13(a). The free contraction of wall thickness (square scatters) is distributed within the band. The fully restrained contraction of the internal dimension (circle scatters) is distributed below the band. The semi-restrained contraction of external dimensions (triangle scatters) is partly in the band and partly below the band. All the measured values of PA show a statistical mean value of 1.45% (Fig. 13(b)), which is lower than that for C1−C8.

It has been reported that the saltation of dimension contraction and release of casting stress occur during the shake-out of sand mold [29], which shows that the constraint of the sand cores plays a major role in restraining the contraction of the casting. Based on this, the contraction of the studied frame in this work is divided into three parts: solidification contraction ($PA_c$), solid contraction ($PA_s$) before (the contraction of this part is recorded as $PA_{bs}$) and after shake-out (the contraction of this part is recorded as $PA_{as}$)), as shown in Fig. 14. The solidification shrinkage ($PA_c$) only occurs on the

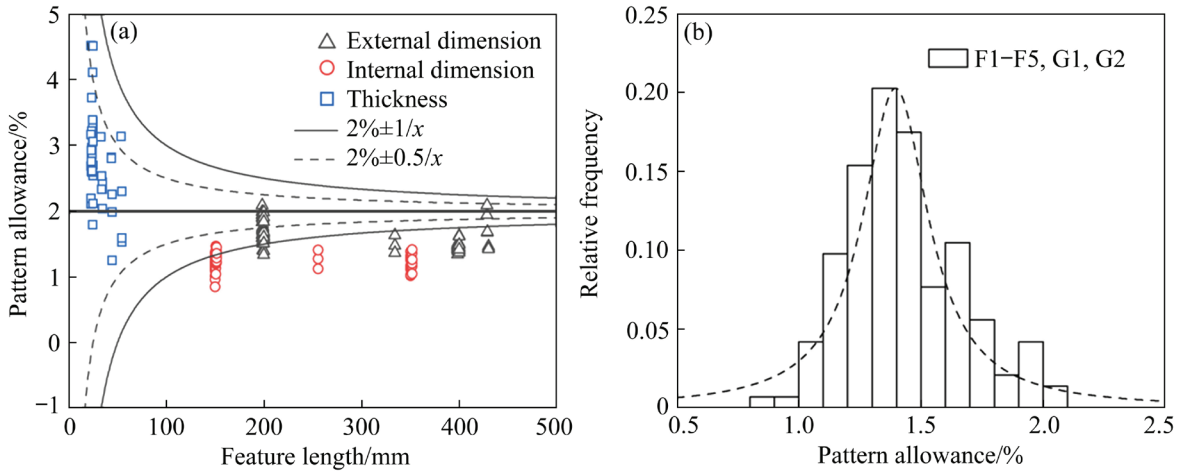


**Fig. 13** Distribution trend of linear shrinkage of hindered structures (a) and statistical results of shrinkage of hindered structures (b)

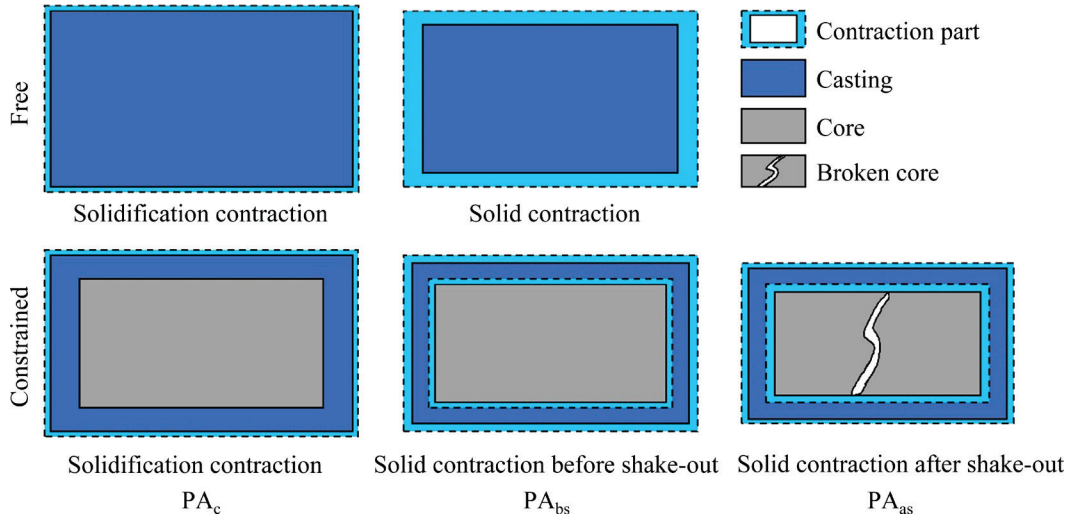


**Fig. 14** Schematic diagram for dimension change under free and restrained contraction

wall thickness, the $PA_{bs}$ is restrained by the sand core obstruction, and the $PA_{as}$ is similar to the free contraction. The measured internal dimensional contraction for the restrained structures equals the sum of solid contraction before and after shake-out ($PA_s = PA_{bs}+PA_{as}$).

The free dimensions of restrained structures (F1−F5, G1, G2), such as wall thickness, exhibit similar contraction law with free structures (C1−C8), but the restrained dimensions, such as external and internal dimensions, exhibit different contraction laws from free structures. However, knowing this gives little help for the pattern dimension design of restrained structures. In order to explore the effect of geometry on restrained contraction, the CVF is introduced.

In order to quantitatively describe the relationship between the contraction and geometric features, envelope density was proposed by CAMPBELL [26] and has achieved certain applications in the prediction of contraction for cast iron and aluminum alloys. The ratio of casting mass to its envelope volume is referred as envelope density, the value of which is dependent on the relative proportion of casting volume and envelope volume. Based on this, the ratio of sand core volume to casting envelope volume is defined as the sand core volume factor (CVF, $f_v$) $f_v = V_{core}/V_{envelope}$. Essentially, the value of CVF represents the degree of constraint induced by sand cores, i.e. the contraction of structure with larger CVF is constrained more sufficiently by sand cores.

The CVF of the restrained structures is listed in Table 3, and the relationship between constrained contraction and CVF is shown in Fig. 15. From Fig. 15, the restrained contractions for internal dimensions of frames (F1−F5, G1 and G2) decline as a function of CVF, $A_P$=1.65−0.706$f_v$. As the value of CVF approaches 0 and 1, two extreme cases, viz. the free contraction and extremely restrained contraction, are worth attention. When CVF equals 0, the fully dense metal casting shows a solid contraction of 1.65%, very close to the value of thermal shrinkage (1.68%, calculated by Eq. (2)) that is an intrinsic parameter of the studied alloy. In contrast, as the value of CVF is infinitely close to 1, the thin-walled box casting has a maximum constraint, and the contraction after shake-out approaches 0.94%.

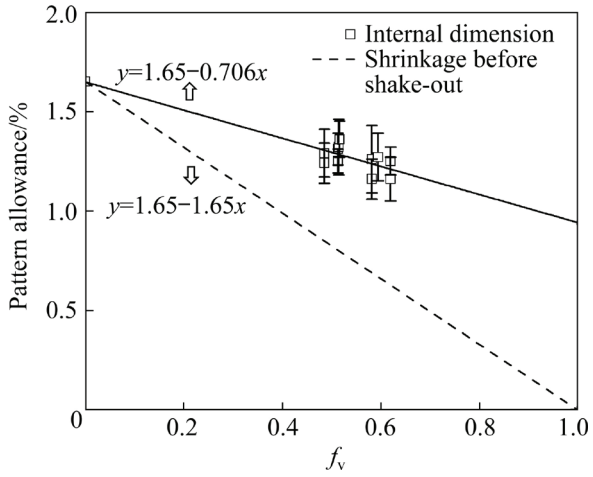


**Fig. 15** Evolution of restrained contraction of frames (F1−F5, G1 and G2) against CVF

It can be further assumed that $PA_{bs}$ (the contraction before shake-out) is 0 at the extreme point of CVF equal to 1 and is linearly correlated with CVF. According to this hypothesis, the evolution of $PA_{bs}$ against CVF is revealed by the dash line in Fig. 15 where the growing interval from $PA_{bs}$ (dash line) to $PA_s$ (solid line) with increasing CVF indicates the accumulating of casting stress. Given this, the correlation between $PA_{bs}$ and CVF, which helps to assess the casting stress and so strategies to protect casting from cold cracking, deserves extra research.

The restrained contraction of frames (F1−F5, G1, G2) is connected with casting geometry by the introduction of CVF and the obtained formula, $A_P$= 1.65%−0.706$f_v$, reflects the influence of both the intrinsic parameter (thermal shrinkage, geometric characteristics) and obstruction induced by sand cores. However, the evolution of radial contraction of hollow cylinders (R4, R5) against CVF is out of the obtained formula (Fig. S3). Extra research work is necessary to find how radial contraction is evolved against the geometry of hollow cylinder.

## 5 Conclusions

(1) For cubic blocks, the value of free contraction confirms the formula: $A_P$=1.95%±1/$x$, where the first item of 1.95% represents the result of solidification contraction and solid contraction.

(2) For the cylinders and cubic blocks with the same volume, the radial contraction for the cylinder is correlated with the $H$/$D$ ratio and exhibits a value about 2 times of free contraction for cubic blocks.

(3) For constrained frames, the free contraction of wall thickness is in accordance with that for free blocks, and the restrained contraction of internal dimensions is determined by the thermal shrinkage and obstruction caused by sand cores, as described in the formula: $A_P$=1.65%−0.706$f_v$.

### CRediT authorship contribution statement

**Rui JIANG:** Conceptualization, Methodology, Investigation, Formal analysis, Writing − Original draft; **Guo-hua WU:** Supervision, Project administration, Writing − Review & editing, Funding acquisition; **He XIE:** Investigation, Writing − Review & editing, Validation; **Xin TONG:** Writing − Review & editing, Validation; **Liang ZHANG:** Supervision, Writing − Review & editing, Validation; **Fang-zhou QI**: Investigation, Visualization; **Wen-cai LIU:** Supervision, Validation; **Ying-jing GENG:** Supervision; **Guang-xiao REN:** Supervision.

### Declaration of competing interest

The authors declare that they have no known competing financial interests or personal relationships that could have appeared to influence the work reported in this paper.

### Acknowledgments

This research was supported by the National Natural Science Foundation of China (Nos. U2037601, 51821001), and Key Basic Research Project of the National Basic Strengthening Plan, China (No. 2022-xxxx-ZD-093-xx).

## Supplementary materials

Supplementary materials in this paper can be found at: http://tnmsc.csu.edu.cn/download/06-p1441-2022-1138-Supplementary_Materials.pdf.

## References


[1] WU Guo-hua, WANG Cun-long, SUN Ming, DING Wen-jiang. Recent developments and applications on high-performance cast magnesium rare-earth alloys [J]. Journal of Magnesium and Alloys, 2021, 9: 1−20.

[2] TONG Xin, WU Guo-hua, EASTON M A, SUN Ming, STJOHN D H, JIANG Rui, QI Fang-zhou. Exceptional grain refinement of Mg−Zr master alloy treated by tungsten inert gas arc re-melting with ultra-high frequency pulses [J]. Scripta Materialia, 2022, 215: 114700.

[3] PANG Song, WU Guo-hua, LIU Wen-cai, ZHANG Liang, ZHANG Yang, CONRAD H, DING Wen-jiang. Influence of pouring temperature on solidification behavior, microstructure and mechanical properties of sand-cast Mg−10Gd−3Y−0.4Zr alloy [J]. Transactions of Nonferrous Metals Society of China, 2015, 25: 363−374.

[4] WANG Xue-zhao, WANG You-qiang, NI Chen-bing, FANG Yu-xin, YU Xiao, ZHANG Ping. Effect of Gd content on microstructure and dynamic mechanical properties of solution-treated Mg−*x*Gd−3Y−0.5Zr alloy [J]. Transactions of Nonferrous Metals Society of China, 2022, 32: 2177−2189.

[5] MEI Jun, LIU Wen-cai, WU Guo-hua, ZHANG Yang, ZHANG Yi-tao, HONG Yi-kai, ZHANG Ruo-xi, XIAO Lü, DING Wen-jiang. Effect of complex melt-refining treatment on microstructure and mechanical properties of sand-cast Mg–10Gd–3Y–0.5Zr alloy [J]. Transactions of Nonferrous Metals Society of China, 2015, 25: 1811−1821.

[6] XIE He, WU Guo-hua, ZHANG Xiao-long, ZHANG Jin-shuo, DING Wen-jiang. The role of Yb content on the microstructural evolution and mechanical characteristics of cast Mg−9Gd−0.5Zn−0.2Zr alloy [J]. Materials Science and Engineering A, 2021, 817: 141292.

[7] LUO Kang, ZHANG Liang, WU Guo-hua, LIU Wen-cai, DING Wen-jiang. Effect of Y and Gd content on the microstructure and mechanical properties of Mg–Y–RE alloys [J]. Journal of Magnesium and Alloys, 2019, 7: 345−354.

[8] NIE Jian-feng. Precipitation and hardening in magnesium alloys [J]. Metallurgical and Materials Transactions A, 2012, 43: 3891−3939.

[9] LIU Wen-cai, JIANG Long-kang, CAO Liang, MEI Jun, WU Guo-hua, ZHANG Song, XIAO Lü, WANG Shao-hua, DING Wen-jiang. Fatigue behavior and plane-strain fracture toughness of sand-cast Mg–10Gd–3Y–0.5Zr magnesium alloy [J]. Materials & Design, 2014, 59: 466−474.

[10] SONG Jiang-feng, SHE Jia, CHEN Dao-lun, PAN Fu-sheng. Latest research advances on magnesium and magnesium alloys worldwide [J]. Journal of Magnesium and Alloys, 2020, 8: 1−41.

[11] LUO A A. Magnesium casting technology for structural applications [J]. Journal of Magnesium and Alloys, 2013, 1: 2−22.

[12] TONG Xin, WU Guo-hua, ZHANG Liang, WANG Ying-xin, LIU Wen-cai, DING Wen-jiang. Microstructure and mechanical properties of repair welds of low-pressure sand-cast Mg–Y–RE–Zr alloy by tungsten inert gas welding [J]. Journal of Magnesium and Alloys, 2022, 10: 180−194.

[13] WANG Quan, XIAO Lü, LIU Wen-cai, ZHANG Hao-hao, CUI Wen-dong, LI Zhong-quan, WU Guo-hua. Effect of heat treatment on tensile properties, impact toughness and plane-strain fracture toughness of sand-cast Mg−6Gd−3Y−0.5Zr magnesium alloy [J]. Materials Science and Engineering A, 2017, 705: 402−410.

[14] GALLES D, BECKERMANN C. Effect of sand dilation on distortions and pattern allowances during steel sand casting [J]. International Journal of Cast Metals Research, 2017, 30: 257−275.

[15] PETERS F, VOIGT R, OU S Z, BECKERMANN C. Effect of mould expansion on pattern allowances in sand casting of steel [J]. International Journal of Cast Metals Research, 2007, 20: 275−287.

[16] ESKIN D G, KATGERMAN L, SUYITNO, MOONEY J F. Contraction of aluminum alloys during and after solidification [J]. Metallurgical and Materials Transactions A, 2004, 35: 1325−1335.

[17] GALLES D, BECKERMANN C. Prediction of distortions and pattern allowances during sand casting of a steel bracket [J]. International Journal of Cast Metals Research, 2017, 30: 133−147.

[18] WANG Wan-long, STOLL H W, CONLEY J G. Rapid tooling guidelines for sand casting [M]. New York: Springer Science & Business Media, 2010.

[19] NAZARETH E S, VOIGT R C, PETERS F E. Dimensional variability of production iron castings [M]. Des Plaines: Amer Foundrymens Soc, 1998.

[20] MKUMBO C S E, NYICHOMBA B B, CAMPBELL J, TIRYAKIOGLU M. Linear contraction of grey iron sand castings [J]. International Journal of Cast Metals Research, 2002, 14: 225−234.

[21] NYICHOMBA B B, CHEYA I M, CAMPBELL J. Linear contraction of ductile iron castings [J]. International Journal of Cast Metals Research, 1998, 11: 179−186.

[22] SVENSSON I L, DUGIC I. Modelling of volumes in cast iron solidification to predict shrinkage and expansion defects [J]. International Journal of Cast Metals Research, 1999, 11: 489−494.

[23] MACHT J P, MAIJER D M, PHILLION A B. A combined numerical–experimental approach to quantify the thermal contraction of A356 during solidification [J]. Metallurgical and Materials Transactions A, 2017, 48: 3370−3376.

[24] NYICHOMBA B B, CAMPBELL J. Linear contraction and residual stress of aluminium alloy sand castings [J]. International Journal of Cast Metals Research, 1998, 11: 163−177.

[25] KOCHAR V. Geometry dependent pattern allowance prediction for castings [D]. Philadelphia: The Pennsylvania State University, 2006: 247.

[26] CAMPBELL J. Complete casting handbook [M]. 2nd ed. Amsterdam: Elsevier, 2015.

[27] MARUMOTO N, KASHIMURA H, YOSHIDA K, TOYODA T, OKANE T, YOSHIDA M. Dynamic measurements of the load on gray cast iron castings and contraction of castings during cooling in furan sand molds [J]. Journal of Materials Processing Technology, 2016, 237: 48−54.
[28] MOTOYAMA Y, INOUE Y, SAITO G, YOSHIDA M. A verification of the thermal stress analysis, including the furan sand mold, used to predict the thermal stress in castings [J]. Journal of Materials Processing Technology, 2013, 213: 2270−2277.
[29] MOTOYAMA Y, TAKAHASHI H, INOUE Y, SHINJI K, YOSHIDA M. Development of a device for dynamical measurement of the load on casting and the contraction of the casting in a sand mold during cooling [J]. Journal of Materials Processing Technology, 2012, 212: 1399−1405.
[30] MOTOYAMA Y, TAKAHASHI H, INOUE Y, SHINJI K, YOSHIDA M. Dynamic measurements of the load on castings and the contraction of castings during cooling in sand molds [J]. Journal of Materials Processing Technology, 2013, 213: 238−244.
[31] GALLES D. Prediction of distortions and pattern allowances in steel sand castings [D]. Iowa City: The University of Iowa, 2016: 118.
[32] MANDAR D. A pattern allowance advisor tool for steel castings [D]. Philadelphia: The Pennsylvania State University, 2005: 293.

# 砂型铸造 Mg−9Gd−3Y−0.5Zr 合金的线收缩

蒋 锐[1]，吴国华[1]，谢 赫[1]，童 鑫[1]，张 亮[1]，戚方舟[1]，刘文才[1]，耿莹晶[2]，任广笑[2]

1. 上海交通大学 材料科学与工程学院 轻合金精密成型国家工程研究中心，
金属基复合材料国家重点实验室，上海 200240；
2. 山西江淮重工有限责任公司，晋城 048000

**摘 要**：研究铸件几何特征对砂型铸造 Mg−9Gd−3Y−0.5Zr(VW93)合金线收缩的影响。利用 3D 扫描仪精确提取自由收缩和受阻收缩砂铸件的尺寸，并用于计算收缩系数。引入砂芯体积与铸件包络体积之比($\gamma$)量化砂芯对铸件收缩的约束程度。通过分析自由收缩系数的统计分布和受阻收缩系数随 $\gamma$ 的变化规律发现，VW93 合金的自由收缩系数为 1.96%，受阻收缩系数随 $\gamma$ 的增大而线性减小，此关系为根据铸件几何结构预测 VW93 合金收缩率提供支持。

**关键词**：自由收缩；受阻收缩；砂型铸造；Mg−9Gd−3Y−0.5Zr 合金

**(Edited by Xiang-qun LI)**